Full-Spectrum Thermal Analysis in Twisted Bilayer Graphene

Wenxiang Liu[1], Yongqiang Wu[2], Yang Hong[3], Bo Hou[4], Jingchao Zhang[5,*], Yanan Yue[1,*]

[1]School of Power and Mechanical Engineering, Wuhan University, Wuhan, Hubei 430072, China

[2]Weichai Power Corporation, Ltd, Weifang 261061, China

[3]School of Chemistry and Biochemistry, Georgia Institute of Technology, Atlanta, GA 30332, USA

[4]Department of Physics and Astronomy, Cardiff University, Cardiff CF24 3AA, UK

[5]NVIDIA AI Technology Center (NVAITC), Santa Clara, CA 95051, USA

ABSTRACT It was recently reported that a magic angle, *i.e.* 1.1º, exists in twisted bilayer graphene which could lead to intrinsic unconventional superconductivity. Variations of the twisting angle between different graphene layers could lead to altered electronic band structures, which gives the peculiar superconductivity phenomenon. Effects of twisting angles on different properties of bilayer graphene need to be comprehensively investigated in order to fully understand its mechanism. In this work, classical molecular dynamics simulations are performed to calculate the interfacial thermal resistance (R) at twisting angles from 0º to 359º. Due to the symmetric structures of the honeycomb lattice, only angles from 0º to 60º is needed but the full spectrum is explored to generate the complete picture of R with θ. It was reported the interfacial thermal resistance changes periodically with twisting angle, with the smallest R values at every 60º starting from 0º and the largest values at every 60º starting from 30º. Phonon density of states and radial distribution functions are calculated to explain the predicted results. Effects of temperature and single-direction, bi-direction tensile strains on the calculated interfacial thermal resistance are also studied. Results in this work contribute to the fundamental understanding of the thermal properties in twisted bilayer graphene and provide reasonable guidelines to its applications in thermal management devices.

*Corresponding Authors. jingchaoz@nvidia.com, yyue@whu.edu.cn

1. Introduction

Single layer graphene which consists of honeycomb structured carbon atoms has been extensively investigated due to its unique properties[1-10]. It exhibits an extraordinarily high thermal conductivity of 2000 W·m/K and its charge carrier mobilities at room temperature can reach 20000 $cm^2/V·s$[11-13]. As a promising material, graphene can be applied in numerous fields such as field effect transistors (FET)[14], optoelectronic devices[15], biosensors[16] and thermal interface materials (TIMs)[17]. At the same time, it derived various 2D materials[18-20] and composite structure[21, 22]. Bohayra *et al.*[22] systematically study the thermal properties of graphene laminates from microscopic level to macroscopic level and found the flake size strongly effects the thermal conductivity. However, due to the lack of a bandgap, its applications in electronic devices are restricted. To remedy this problem, graphene nanoribbons (GNRs)[23] and bilayer graphene[24] are explored. By applying a vertical electric field, the bandgap of bilayer graphene can be controlled which opens possibilities for more applications[25]. Recently, superconductivity is observed in twisted bilayer graphene (T-BLG) at a magical angle of 1.1 degree[26]. By applying more pressure, the superconductivity in T-BLG is found in even higher rotation angles[27, 28]. Those results inspire the fundamental studies in their electrical and thermal properties and possible applications of T-BLG.

Both experimental and theoretical studies have been performed to explore the peculiar properties of twisted bilayer graphene. By using the continuum model, Tarnopolsky *et al.*[29] reported the perfect flattening of entire band which can be a new feature of superconductivity in T-BLG with certain angles. More magic angles were predicted by theoretical analyses and remarkable asymptotic periodicity have been found. In addition, the peculiar Moiré pattern by

rotating the graphene not only affects the electrical properties but also the phonon transportation. Wu *et al.*[30] explored the conductivity in T-BLG by using the theory of phonon-mediated paring and discussed the combination of the local repulsion and the phonon attraction. Superconducting transition temperatures can be explained using the phonon attractions between *s*-wave and *d*-wave channels. Also using continuum model, Cocemasov *et al.*[31] systematically analyzed the phonon modes in T-BLG. A more complicated phonon dispersion was calculated due to the rotation of the bottom and top layer. Interestingly, different phonon branches which called hybrid folded phonons were observed in phonon dispersion of T-BLG. Wang *et al.*[32] synthetically studied the dependence of folded phonon frequency on the rotation angle of T-BLG and found the folded phonon frequency descend with the increase of the twisting angles in Raman spectra. The phonon frequency is consistent with *ab initio* calculation.

The thermal properties of T-BLG have also been explored in previous literature. Li *et al.*[33] measured the thermal conductivity of T-BLG using optothermal Raman technique. It was reported that the thermal conductivity of T-BLG decreases compared to monolayer graphene. The reason ascribes to numerous folded phonon branches which enhance the phonon Umklapp scattering. Nie *et al.*[34] employed non-equilibrium molecular dynamics (NEMD) to investigate the thermal conductivity of T-BLG. Different temperatures, angles and the number of layers were considered. A downward tendency with the increasing temperature and the symmetric results of different angles have found. Also using NEMD, Li *et al.*[35] investigated the dependence of lattice constant on thermal conductivity in misoriented bilayer graphene and found the reducing of thermal conductivity due to the reduction of Brillouin zone which result in the enhancement of Umklapp scattering. Despite the abovementioned results, full-spectrum

thermal analyses on the interfacial thermal resistance of T-BLG have not been reported. This is an important topic to help understand the thermal properties of T-BLG and therefore is urgently needed.

In this work, classical molecular dynamics (MD) simulation is performed to investigate the interfacial thermal transport across T-BLG interface. Impacts of rotation angle, system temperature and tensile strength are considered. Instead of using the traditional NEMD approach, a transient pump-probe method is employed, which mimics the thermal reflectance method and can directly compare to experimental results[36-40]. Radius distribution function (RDF), phonon density of state (PDOS) and overlap factor are used to help understand the calculated results. This article is oriented as below. Section two describes the configurations of the T-BLG system and the MD simulation setup. The trainset pump-probe approach and the analyses methods are explained in detail. Section three reports the calculated interfacial thermal resistance under different impact factors and discusses the mechanism leading to the reported results. The last section summarizes the findings of this work.

2. Methodology

The atomic systems of T-BLG were created using two parallel monolayer graphene stacked in AA pattern and are labeled as top and bottom, respectively. The periodic lattice structure and unit cell size are changed to obtain different twisting angles. For example, a unit cell with twisting angles of 21.8° contains 28 carbon atoms, and for 13.2°, it contains 76 atoms[31]. Therefore, during the model creation, the size of bottom layer is larger than that of the top layer. The bottom layer was rotated with desired angles. After rotation, the bottom layer

was tailored to match the size of the top layer. Top views of T-BLG at different twisting angles of 0°, 15°, 30° and 60°are shown in Fig. 1. The cross-sectional area of the pristine T-BLG without twisting angles is 100.01×99.17 (x×y) Å^2. The initial distance between top and bottom layers is set as 3.35 Å. A fixed boundary condition is used in both x and y directions and free boundary condition is used in the out-of-plane z direction.

All MD simulations in this work are performed by the open source Large-scale Atomic/Molecular Massively Parallel Simulator (LAMMPS)[41]. The optimized Tersoff empirical potential[42] is used to describe the in-plane C-C interactions in this study, which is expressed as:

$$E = \frac{1}{2}\sum_{i}\sum_{i\neq j} V_{ij} \tag{1}$$

$$V_{ij} = f_C(r_{ij})\left[f_R(r_{ij}) + b_{ij} f_A(r_{ij}) \right] \tag{2}$$

where V_{ij} is the potential energy and f_R represents the two-body term. f_A includes three-body interactions. Meanwhile, the interaction between the top layer and the bottom layer is modeled as van der Waals (vdW) interaction using the Lennard-Jones potential which is described as:

$$V(r) = 4\chi\varepsilon[(\frac{\sigma}{r})^6 - (\frac{\sigma}{r})^{12}] \tag{3}$$

where χ represents the coupling factor and ε and σ are the energy parameter and distance parameter separately. In this study, value of ε and σ are extracted from the Universal force field (UFF) table[43] where $\varepsilon_{C\text{-}C}$ = 4.56 meV, $\sigma_{C\text{-}C}$ = 3.431 Å. The cutoff distance is set as 12.5 Å and each time step is 0.5 fs.

The interfacial thermal resistance is calculated by a transient pump-probe method. Its mechanism is described as following. The hybrid system is initially placed in a Nosé–Hoover

thermostat at 300 K for relaxation. Then the microcanonical ensemble is used to maintain the conservation of the total energy for 50 ps. Once the system reaches thermal equilibrium, a pulsed energy of 50 fs was applied to the top layer. Immediately after the thermal pulse, temperature of the top layer reaches ~546 K while the bottom layer remains at 300 K. Once the temperature difference is established, thermal resistance can be calculated by the equation[44]:

$$\frac{dE_{top}}{dt} = A \cdot (T_{bot} - T_{top}) / R \tag{4}$$

where E_{top} is the total energy of the top graphene, A is area and T_{top} and T_{bot} are the temperatures of the top graphene and the bottom graphene separately. R is the value of the thermal resistance. For example, temperature and energy profiles with time are shown in Fig. 2(a) and Fig. 2(b) respectively. The black line represents the temperature of the top layer and the red line represents the temperature of the bottom layer in Fig. 2(a). Temperature difference decreases with time and converges after 90 ps. The integral form of Eq (4) is described as:

$$E_t = E_0 + (A / R) \cdot \int_0^t (T_{bot} - T_{top}) dt \tag{5}$$

where E_t is the top graphene energy which varies with time and E_0 is the initial energy. Energy relaxation with time is fitted and the result is shown in the yellow line in Fig. 2(b). The fitting profile soundly matches the energy outputs from MD simulation, which validates this approach for R extractions. It is worth noting that the value of E_0 in the fitting curve is different from the value in the blue line. In addition, R value at each angle is averaged from 5 independent simulations.

Phonon density of states is an important metric in understanding the calculated R results and it can be calculated by performing fast Fourier transform (FFT) on the velocity autocorrelation functions (VACF):

$$F(\omega)=\frac{1}{\sqrt{2\pi}}\int_{-\infty}^{+\infty}\frac{\langle v(0)\cdot v(t)\rangle}{\langle v(0)\cdot v(0)\rangle}e^{i\omega t}dt \tag{6}$$

where $\langle v(0)\cdot v(t)\rangle$ represent ensemble average of velocity and F is the phonon numbers with certain frequency. A larger value of F means more numerous phonons occupied at given ω.

3. Results and Discussion

3.1 Effect of twisting angles

The interfacial thermal resistance at different twisting angles is first explored and the calculated results from 0° to 359° are shown in Fig. 3. The radial distribution of the computed results has a maple leaf shape. A periodic range of 60° can be observed which is consistent with the hexagonal honeycomb structure of graphene shown in Fig. 1. The R value increases from 2.74×10^{-8} K·m^2/W at 0° to 9.40×10^{-8} K·m^2/W at 30°. After attaining the summit, the R value decreases to 3.91×10^{-8} K·m^2/W at 60°. The difference of the R value at 0° and 60° ascribes to the slight drift of atomic coordinates because of the rotation which can be observed in Fig. 1. In addition, the increase and decrease of the R values are nonlinear with the change of twisting angles. Especially near the 0° and 60°, sharper up and down trends can be noticed. Such nonlinear tendency can be found in other structures, such as graphene/hexagonal boron nitride van der Waals (vdW) heterostructure[45]. A statistical analysis is performed, and the results are shown in Fig. 4. Frequency distribution histogram of thermal resistance reveals the abovementioned characteristics. Most of the R values fall into the range of 6×10^{-8} K m^2/W to 8×10^{-8} K m^2/W and a small number of values distributes in other ranges. The long tails of the normal distribution of R values certify the sudden changes near the 0° and 60°.

Phonon behaviors are analyzed to explain the thermal transport at the T-BLG interface.

Compared with the pristine bilayer graphene, lattice structures can change dramatically due to the rotation which result in the increasing number of phonon branches[31]. More complicated phonon branches and flattened curves can be observed in phonon energy dispersion which lead to slower group velocity. In addition, the frequency shift of the flexural phonons weakens the phonon transportation across the interface, which results in the increase of thermal resistance. Radius distribution function (RDF) is calculated to help explain the calculated interfacial thermal resistance, and the results are shown in Fig. 5. In this study, RDF is calculated between the top the bottom carbon atoms. A larger value of *g(r)* represents a denser surrounding on the central atom which indicates more atoms contributing to the thermal transportation. In addition, the nonzero value of *g(r)* at the first given radius shows the distance between the top layer and bottom layer. It is observed that the difference of distance is slight, but the *g(r)* value is consistent with the results of thermal resistance which the largest value at 0°, following by 15° and 30°.

Moreover, to better understand the variations of thermal resistance at different twisting angles, PDOS is calculated and the results are shown in Fig. 6. Only the cross-plane flexural phonons which directly contribute to the interfacial thermal transport are considered in this work[46]. A much softer PDOS can be observed with the twisting angles varying from 0° to 30° which means lower phonon group velocities. The overlap of PDOS is an important factor to help understand the interfacial thermal resistance. To quantitatively explain the result of thermal resistance, an overlap factor (*S*) is calculated and expressed as:

$$S = \frac{\int_{-\infty}^{+\infty} F_1(\omega) F_2(\omega) d\omega}{\int_{-\infty}^{+\infty} F_1(\omega) d\omega \int_{-\infty}^{+\infty} F_2(\omega) d\omega} \tag{7}$$

where F_1 and F_2 are PDOS of different layer. A larger value of overlap factor represents stronger phonon couplings between the bottom and top layers which can lead to reduced thermal resistance. The overlap areas are shaded in Fig. 6 and overlap factor values of T-BLG with twisting angles of 0°, 15° and 30° are 0.0319, 0.0295 and 0.0286 respectively. The decrease of S indicates that the increasing twisting angle weakens the thermal transportation across the interface which caused the increase of thermal resistance.

3.2 Effects of temperature on interfacial thermal resistance

Temperature is an important factor which should be considered in practical applications of thermal interface materials. Effect of temperature on R is shown in Fig. 7. Different values of temperature from 100 K to 500 K are evaluated and different twisting angles are also considered which are plotted in different colors. A monotonic decreasing trend of R with increasing temperature is observed for all twisting angles considered. The R values of T-BLG with twisting angles of 0° decrease from 4.50×10^{-8} K m^2/W at 100K to 1.93×10^{-8} K m^2/W at 500 K. For 30°, the R values decrease from 1.61×10^{-7} K m^2/W to 7.74×10^{-8} K m^2/W, which reveals the strong temperature effects on T-BLG[34]. In addition, for all temperature values, the calculated thermal resistance is symmetric at 30°and a slight difference exists at 0° and 60° which is consistent with the Fig. 3.

Both experimental and simulated studies have revealed that the increasing temperature can decrease the thermal resistance and the reasons have been discussed extensively[44, 47-49]. Low-frequency phonons play an important role in interfacial thermal transport. With the increase of temperature, more high-frequency phonons are activated which make the PDOS spectrum broader. On the other hand, Umklapp scattering is enhanced which makes high-

frequency phonons may break down into larger numbers of low-frequency phonons. The increasing number of low-frequency phonons directly facilitate the cross-plane thermal transport. Meanwhile, the three phonon scatterings enhance the coupling of different phonon branches which also result in the decrease of *R*.

3.3 Effects of single-direction and bi-direction tensile strains on *R*

Since graphene can be used as flexible material given its unique mechanical properties, it is common that strain exist in bilayer graphene due to constraints induced during assembly. Thus, it is important to investigate the effects of strain on thermal resistance of T-BLG. Effects of tensile strains on interfacial thermal resistance are illustrated in Fig. 8(a)~(c) for tensile strain in the (a) *x* direction, (b) *y* direction and (c) bi-direction (*x&y*). Different twisting angles of 0°, 15° and 30° are depicted in different colors. An obvious monotonic upward tendency can be observed in Fig. 8(a)~(c). This tendency is consistent with the previous finding in strain effects on the thermal properties of 2D-materials[50]. The reason of the increase of *R* value with the tensile strains attributes to the bond length elongation that leads to the weakened reaction of the carbon atoms[50, 51]. PDOS is also calculated to understand this tendency. The PDOS of T-BLG at 0° with strain ratios of 1 and 1.08 are illustrated in Fig. 9. The tensile strains are applied in both the *x* and *y* directions. Compared with Fig. 9(a) and Fig. 9(b), a lower peak value and a narrower phonon frequency range are observed at strain ratio of 1.08, which means slow phonon group velocity and results in greater thermal resistance[52]. Phonon softening can be observed in 2D materials with stretch in the past studies[53, 54] and the softened phonons will lead to smaller phonon group velocities which are consistent with the PDOS calculated in this work. Furthermore, the calculated overlap factors provide a quantitative explanation. The overlap

factor values of T-BLG with twisting angle of 0° which stain ratio equal to 1 and 1.08 are 0.032 and 0.031 separately.

Compared to single-direction stretching, bi-direction tensile strains have stronger effects on the predicted interfacial thermal resistance. For 0°, 15° and 30°, the *R* values increase from 2.82×10^{-8} to 4.66×10^{-8} K m^2/W, 6.92×10^{-8} to 1.01×10^{-7} K m^2/W, and 9.36×10^{-8} to 1.45×10^{-7} K m^2/W, respectively, which corresponds to increasing ratios of 65.25%, 31.49% and 54.9%. On the other hand, single-direction tensile strains only cause increase ratios of 19.1%, 18.6% and 19.65%, respectively. The differences can be accounted to the unit cell deformation due to the varying tensile strengths and tensile directions.

4. Conclusion

A transient pump-probe method is used in this work to systematically investigate the thermal transport at the T-BLG interface. The effects of twisting angle, system temperature, and tensile strain on interfacial thermal resistance are comprehensively investigated. Symmetrical *R* results with a periodic length of 60° are observed. The calculated *R* value increases from 2.74×10^{-8} K m^2/W at 0° to 9.40×10^{-8} K m^2/W at 30°. The PDOS and RDF are calculated to help understand the results. It is found that the thermal transportation across the interface was weakened from 0° to 30° due to slower phonon velocities and larger layer distances due to rotations, which result in increased thermal resistance. Meanwhile, the *R* value decrease monotonously with the temperature owing to larger phonon populations and stronger phonon scatterings across the interface. On the other hand, in-plane tensile strains lead to increased *R* values. Compared with single-direction tensile strains, bi-direction strains have a

stronger impact in cross-plane thermal transport. Our results shed some light on understanding the interfacial thermal transport in T-BLG and provide helpful guidelines in its appliances.

ACKNOWLEDGEMENT

Y. Yue acknowledges the support from the National Natural Science Foundations of China (No. 52076156), National Key Research and Development Program (No. 2019YFE0119900) and Fundamental Research Funds for the Central Universities (No. 2042020kf0194).

References

1. A. A. Balandin, *Nat Mater*, 2011, **10**, 569-581.
2. C. Lee, X. Wei, J. W. Kysar and J. Hone, *Science*, 2008, **321**, 385-388.
3. X. Dong, C. Y. Su, W. Zhang, J. Zhao, Q. Ling, W. Huang, P. Chen and L. J. Li, *Phys Chem Chem Phys*, 2010, **12**, 2164-2169.
4. K. S. Novoselov, A. K. Geim, S. V. Morozov, D. Jiang, Y. Zhang, S. V. Dubonos, I. V. Grigorieva and A. A. Firsov, *Science*, 2004, **306**, 666-669.
5. F. Schedin, A. K. Geim, S. V. Morozov, E. W. Hill, P. Blake, M. I. Katsnelson and K. S. Novoselov, *Nat Mater*, 2007, **6**, 652-655.
6. X. Wang, H. Fan, D. Han, Y. Hong and J. Zhang, *Nanotechnology*, 2021, **32**, 215404.
7. Y. Hong, D. Han, B. Hou, X. Wang and J. Zhang, *International Journal of Heat and Mass Transfer*, 2021, **171**, 121073.
8. Y. Hong, B. Hou, H. Jiang and J. Zhang, 2020, **10**, e1450.
9. Z. Zhang, Y. Hong, B. Hou, Z. Zhang, M. Negahban and J. Zhang, *Carbon*, 2019, **148**, 115-123.
10. H. Yang, Z. Zhang, J. Zhang and X. C. Zeng, *Nanoscale*, 2018, **10**, 19092-19099.
11. K. S. Novoselov, A. K. Geim, S. V. Morozov, D. Jiang, M. I. Katsnelson, I. V. Grigorieva, S. V. Dubonos and A. A. Firsov, *Nature*, 2005, **438**, 197-200.
12. Y. Zhang, Y. W. Tan, H. L. Stormer and P. Kim, *Nature*, 2005, **438**, 201-204.
13. S. V. Morozov, K. S. Novoselov, M. I. Katsnelson, F. Schedin, D. C. Elias, J. A. Jaszczak and A. K. Geim, *Phys Rev Lett*, 2008, **100**, 016602.
14. I. Meric, M. Y. Han, A. F. Young, B. Ozyilmaz, P. Kim and K. L. Shepard, *Nat Nanotechnol*, 2008, **3**, 654-659.
15. Q. Bao and K. P. Loh, *ACS Nano*, 2012, **6**, 3677-3694.
16. I. Novodchuk, M. Bajcsy and M. Yavuz, *Carbon*, 2021, **172**, 431-453.
17. V. Goyal and A. A. Balandin, *Applied Physics Letters*, 2012, **100**, 073113.
18. B. Mortazavi, O. Rahaman, T. Rabczuk and L. F. C. Pereira, *Carbon*, 2016, **106**, 1-8.
19. A. Bafekry, C. Stampfl, B. Akgenc, B. Mortazavi, M. Ghergherehchi and C. V. Nguyen, *Phys Chem Chem Phys*, 2020, **22**, 6418-6433.
20. B. Mortazavi, M. Makaremi, M. Shahrokhi, M. Raeisi, C. V. Singh, T. Rabczuk and L. F. C. Pereira, *Nanoscale*, 2018, **10**, 3759-3768.
21. B. He, B. Mortazavi, X. Zhuang and T. Rabczuk, *Composite Structures*, 2016, **152**, 939-946.
22. B. Mortazavi and T. Rabczuk, *Carbon*, 2015, **85**, 1-7.
23. Y. W. Son, M. L. Cohen and S. G. Louie, *Phys Rev Lett*, 2006, **97**, 216803.
24. B. N. Szafranek, D. Schall, M. Otto, D. Neumaier and H. Kurz, *Nano Lett*, 2011, **11**, 2640-2643.
25. E. V. Castro, K. S. Novoselov, S. V. Morozov, N. M. Peres, J. M. dos Santos, J. Nilsson, F. Guinea, A. K. Geim and A. H. Neto, *Phys Rev Lett*, 2007, **99**, 216802.
26. Y. Cao, V. Fatemi, S. Fang, K. Watanabe, T. Taniguchi, E. Kaxiras and P. Jarillo-Herrero, *Nature*, 2018, **556**, 43-50.
27. M. Yankowitz, S. Chen, H. Polshyn, Y. Zhang, K. Watanabe, T. Taniguchi, D. Graf, A. F. Young and C. R. Dean, *Science*, 2019, **363**, 1059-1064.
28. M. Yankowitz, J. Jung, E. Laksono, N. Leconte, B. L. Chittari, K. Watanabe, T.

Taniguchi, S. Adam, D. Graf and C. R. Dean, *Nature*, 2018, **557**, 404-408.
29. G. Tarnopolsky, A. J. Kruchkov and A. Vishwanath, *Phys Rev Lett*, 2019, **122**, 106405.
30. F. Wu, A. H. MacDonald and I. Martin, *Phys Rev Lett*, 2018, **121**, 257001.
31. A. I. Cocemasov, D. L. Nika and A. A. Balandin, *Physical Review B*, 2013, **88**, 035428.
32. Y. Wang, Z. Su, W. Wu, S. Nie, N. Xie, H. Gong, Y. Guo, J. Hwan Lee, S. Xing, X. Lu, H. Wang, X. Lu, K. McCarty, S.-s. Pei, F. Robles-Hernandez, V. G. Hadjiev and J. Bao, *Applied Physics Letters*, 2013, **103**, 123101.
33. H. Li, H. Ying, X. Chen, D. L. Nika, A. I. Cocemasov, W. Cai, A. A. Balandin and S. Chen, *Nanoscale*, 2014, **6**, 13402-13408.
34. X. Nie, L. Zhao, S. Deng, Y. Zhang and Z. Du, *International Journal of Heat and Mass Transfer*, 2019, **137**, 161-173.
35. C. Li, B. Debnath, X. Tan, S. Su, K. Xu, S. Ge, M. R. Neupane and R. K. Lake, *Carbon*, 2018, **138**, 451-457.
36. N. N. Nedyalkov, S. E. Imamova, P. A. Atanasov, R. A. Toshkova, E. G. Gardeva, L. S. Yossifova, M. T. Alexandrov and M. Obara, *Applied Surface Science*, 2011, **257**, 5456-5459.
37. X. Wei, T. Zhang and T. Luo, *ACS Energy Letters*, 2017, **2**, 2283-2292.
38. Y. Yue, J. Zhang and X. Wang, *Small*, 2011, **7**, 3324-3333.
39. J. Zhang, Y. Wang and X. Wang, *Nanoscale*, 2013, **5**, 11598-11603.
40. J. Zhang, Y. Hong and Y. Yue, 2015, **117**, 134307.
41. s. plimpion, *Journal of computational physics*, 1995, **117**, 1-19.
42. L. Lindsay and D. A. Broido, *Physical Review B*, 2010, **81**, 205441.
43. A. K. Rappe, C. J. Casewit, K. S. Colwell, W. A. Goddard and W. M. Skiff, *J Am Chem Soc*, 1992, **114**, 10024-10035.
44. J. Zhang, Y. Hong, Z. Tong, Z. Xiao, H. Bao and Y. Yue, *Phys Chem Chem Phys*, 2015, **17**, 23704-23710.
45. W. Ren, Y. Ouyang, P. Jiang, C. Yu, J. He and J. Chen, *Nano Lett*, 2021, **21**, 2634–2641.
46. X. Gu, Y. Wei, X. Yin, B. Li and R. Yang, *Reviews of Modern Physics*, 2018, **90**, 041002.
47. D. Han, X. Wang, W. Ding, Y. Chen, J. Zhang, G. Xin and L. Cheng, *Nanotechnology*, 2019, **30**, 075403.
48. T. Li, Z. Tang, Z. Huang and J. Yu, *Carbon*, 2016, **105**, 566-571.
49. H. Gu, J. Wang, X. Wei, H. Wang and Z. Li, *Nanotechnology*, 2020, **31**, 505703.
50. J. Chen, J. H. Walther and P. Koumoutsakos, *Nano Lett*, 2014, **14**, 819-825.
51. K. Einalipour Eshkalak, S. Sadeghzadeh and F. Molaei, *The Journal of Physical Chemistry C*, 2020, **124**, 14316-14326.
52. Y. Hong, J. Zhang and X. C. Zeng, *Nanoscale*, 2018, **10**, 4301-4310.
53. F. Liu, P. Ming and J. Li, *Physical Review B*, 2007, **76**, 064120.
54. H. Xie, T. Ouyang, É. Germaneau, G. Qin, M. Hu and H. Bao, *Physical Review B*, 2016, **93**, 075404.

List of Figures

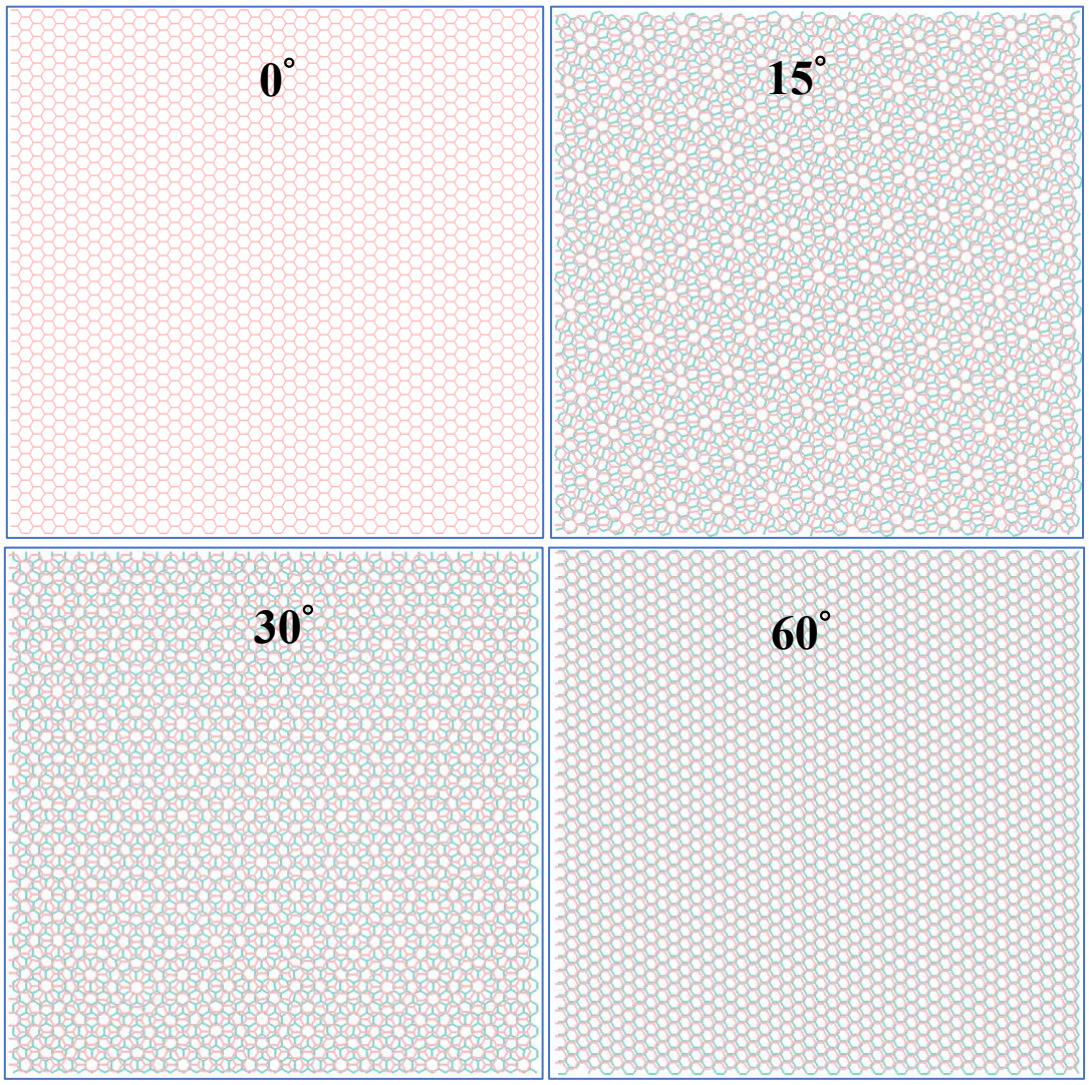

Figure 1. Atomic configurations of twisted bilayer at different in-plane twisting angles ranging from 0º to 60º.

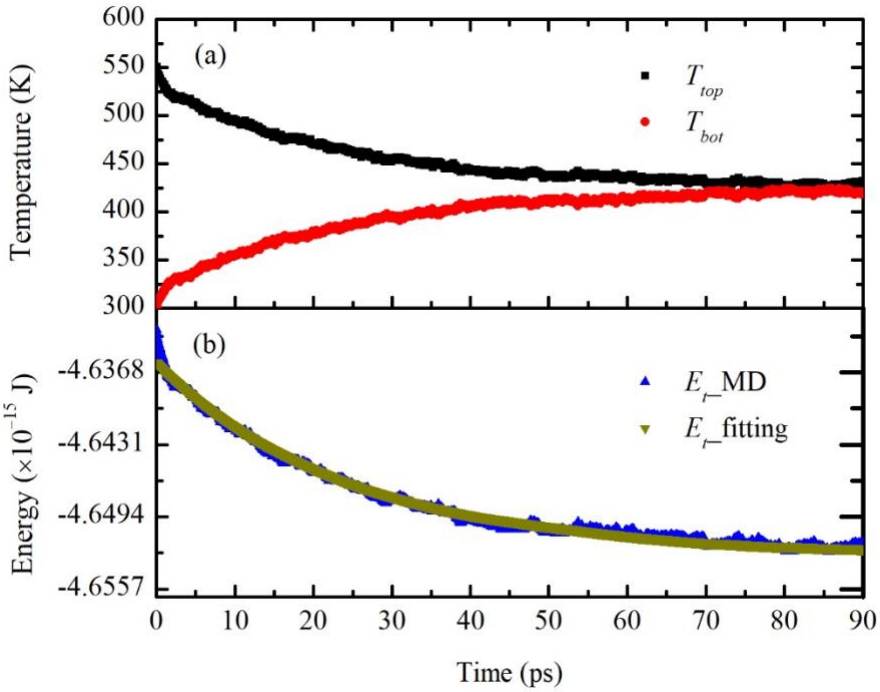

Figure 2. Schematics of the transient heating method for interfacial thermal resistance extraction. (a) Temperature profiles of top and bottom layers of graphene. (b) MD generated energy relaxation and the fitting curve using least square method.

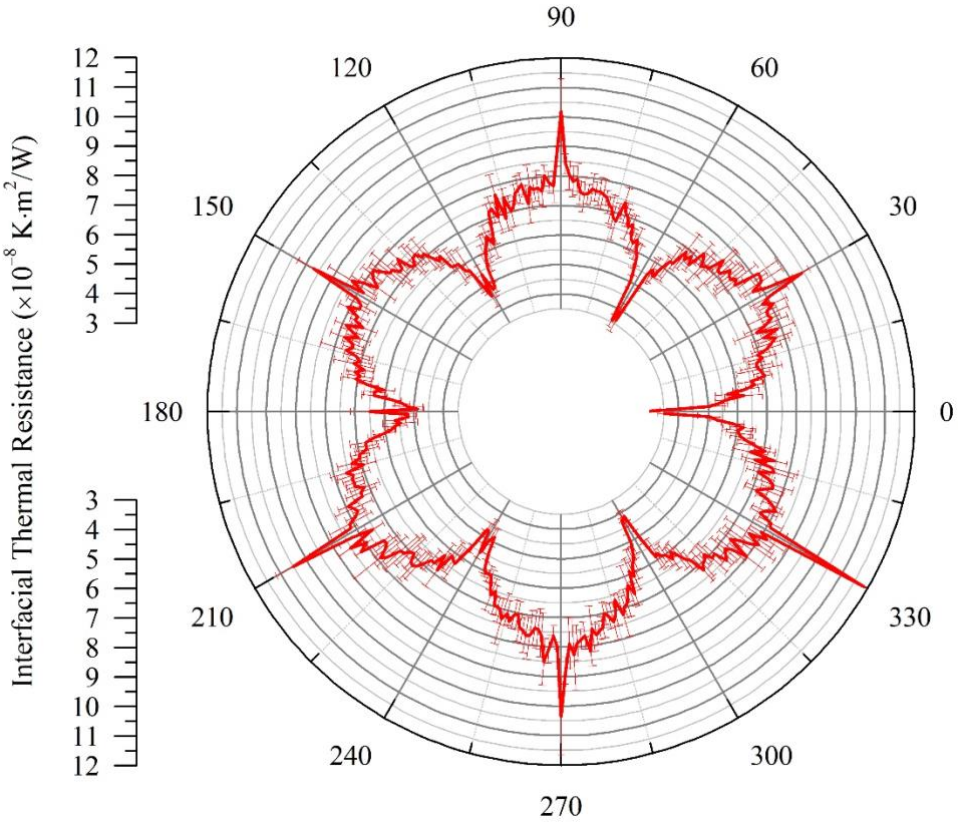

Figure 3. Interfacial thermal resistance of twisted bilayer graphene at all angles from 0º to 359º. The *R* value at each angle is averaged from 5 independent simulations with different initial conditions and the error bar stands for standard deviation.

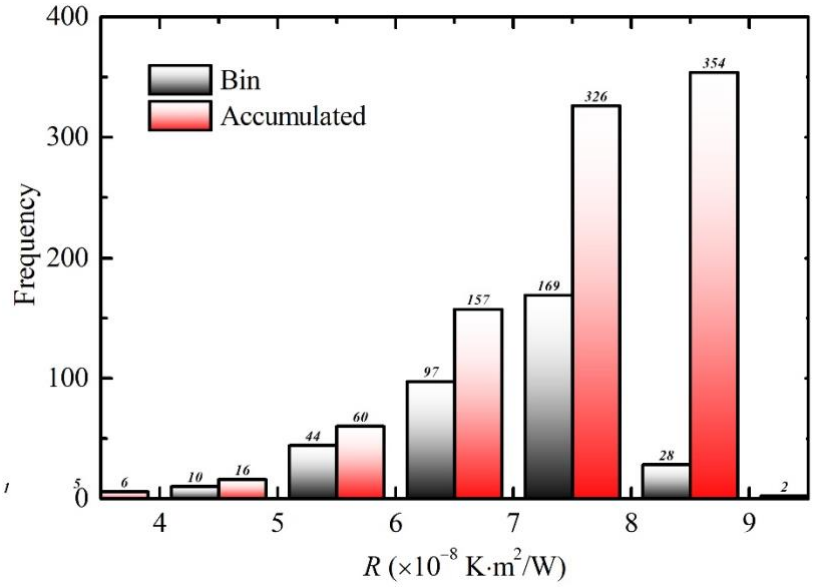

Figure 4. Statistically analyses of the calculated interfacial thermal resistance results at all angles. It can be observed that the majority of R values fall in the range of 7.0×10^{-8} to 8.0×10^{-8} W·m^2/K.

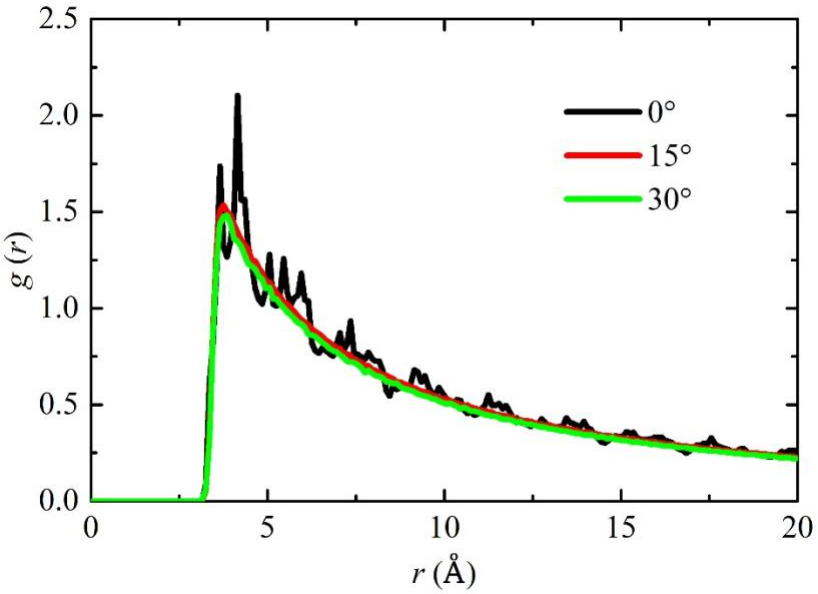

Figure 5. Radial distribution functions at different twisting angles. The largest $g(r)$ is at 0º, followed by 15º, and the smallest $g(r)$ value is at 30º, which is consistent with the results shown in Fig. 3.

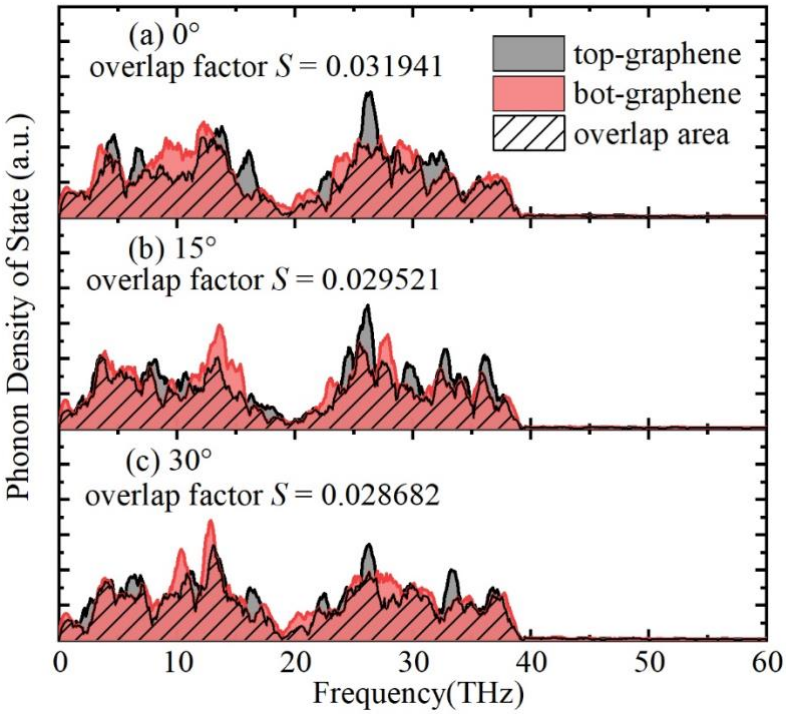

Figure 6. Phonon density of states at different twisting angles. The overlap factor decreases monotonically with increasing twisting angle, indicating weakened phonon couplings and increased interfacial thermal resistance.

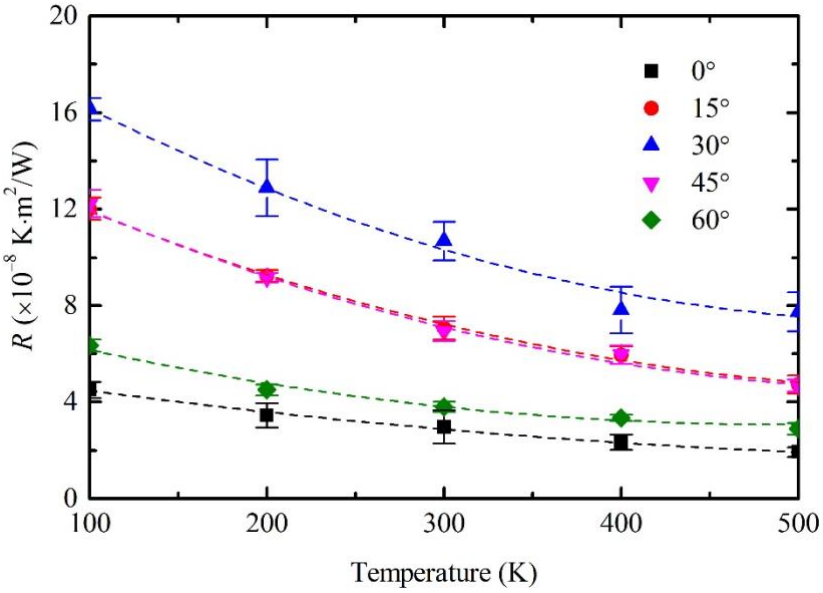

Figure 7. Effects of temperature on interfacial thermal resistance at different twisting angles from 0º to 60º.

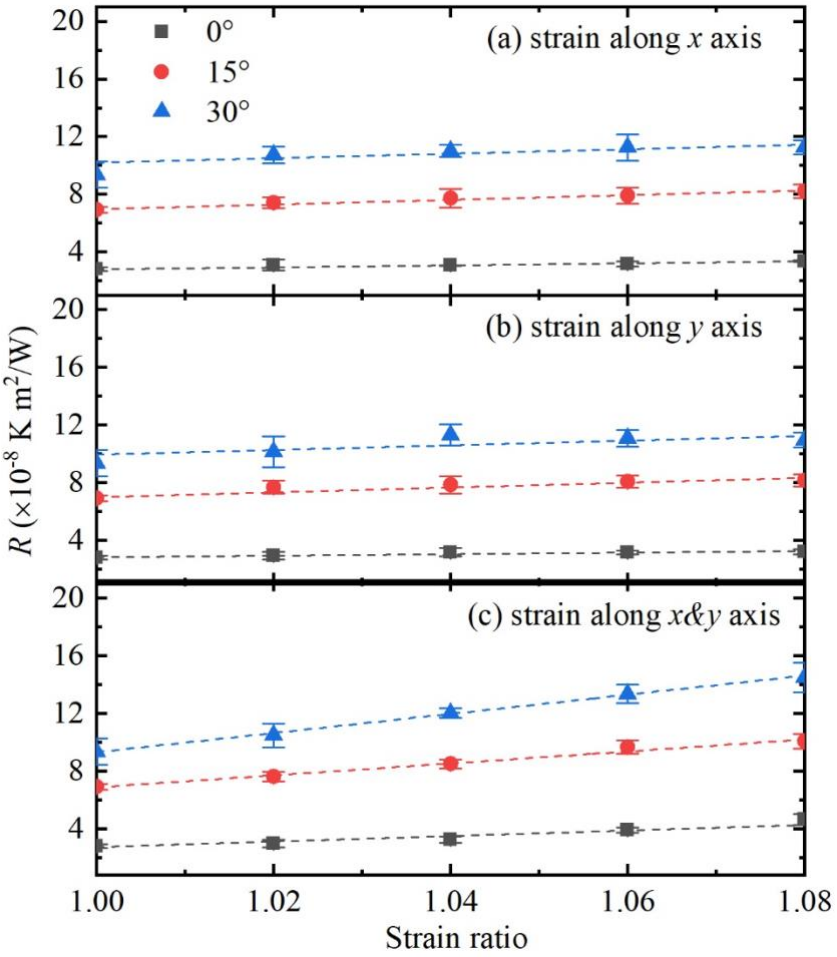

Figure 8. Effects of single direction and bi-direction tensile strains on interfacial thermal resistance at different twisting angles.

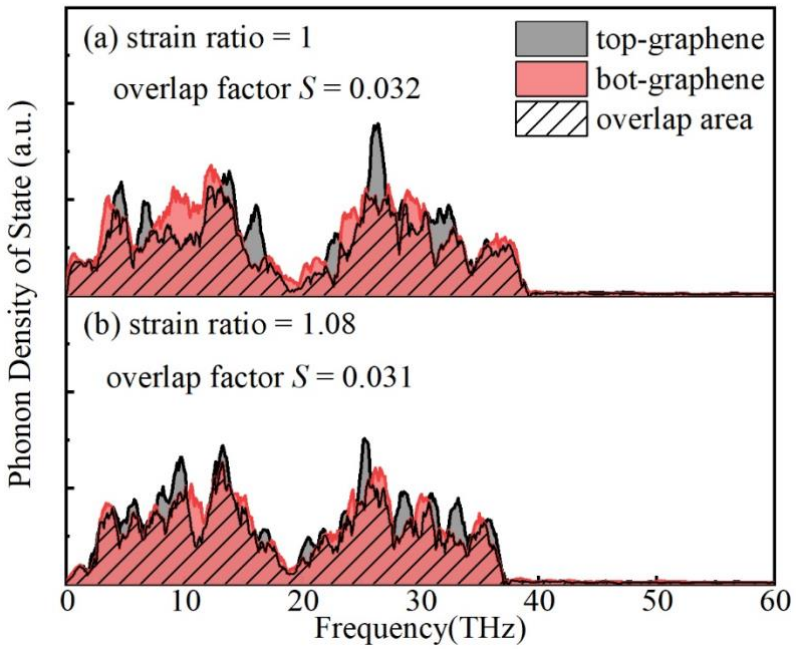

Figure 9. Phonon density of states at different strain ratios. The overlap factor decreases with increasing strain values.